

Firebrand burning under wind: an experimental study

Weidong Yan^{A,B}, Naian Liu^{A,B,*}, Hong Zhu^{A,B,*} , Haixiang Chen^{A,B} , Xiaodong Xie^{A,B}, Wei Gao^{A,B}  and Zhihao Du^{A,B}

For full list of author affiliations and declarations see end of paper

***Correspondence to:**

Naian Liu
 State Key Laboratory of Fire Science,
 University of Science and Technology of
 China, Hefei, Anhui 230026, China
 Email: liunai@ustc.edu.cn

Hong Zhu
 State Key Laboratory of Fire Science,
 University of Science and Technology of
 China, Hefei, Anhui 230026, China
 Email: zhuh15@ustc.edu.cn

Received: 19 September 2023

Accepted: 15 March 2024

Published: 12 April 2024

Cite this: Yan W *et al.* (2024) Firebrand burning under wind: an experimental study. *International Journal of Wildland Fire* 33, WF23151. doi:10.1071/WF23151

© 2024 The Author(s) (or their employer(s)). Published by CSIRO Publishing on behalf of IAWF.

This is an open access article distributed under the Creative Commons Attribution-NonCommercial-NoDerivatives 4.0 International License ([CC BY-NC-ND](https://creativecommons.org/licenses/by-nc-nd/4.0/))

OPEN ACCESS

ABSTRACT

Background. Spot fires play a significant role in the rapid spread of wildland and wildland–urban interface fires. **Aims.** This paper presents an experimental and modelling study on the flaming and smouldering burning of wood firebrands under forced convection. **Methods.** The firebrand burning experiments were conducted with different wind speeds and firebrand sizes. **Key results.** The burning rate of firebrands under forced convection is quantified by wood pyrolysis rate, char oxidation rate and a convective term. The firebrand projected area is correlated with firebrand diameter, char density, wind speed, and flaming or smouldering burning. A surface temperature model is derived in terms of condensed-phase energy conservation. We finally establish a simplified firebrand transport model based on the burning rate, projected area and surface temperature of firebrands. **Conclusion.** The mass loss due to wood pyrolysis is much greater than that due to char oxidation in self-sustaining burning. The burning rate is proportional to $U^{1/2}$, where U is wind speed. The projected area for flaming firebrands decreases more rapidly than that for smouldering ones. The firebrand surface temperature is mainly determined by radiation. **Implications.** Knowledge about firebrand burning characteristics is essential for predicting the flight distance and trajectory in firebrand transport.

Keywords: burning rate, firebrand density, firebrands, flaming and smouldering, forced convection, projected area, surface temperature, transport trajectory.

Introduction

Spot fire denotes the phenomenon that firebrands (e.g., burning barks and twigs) are lofted by the buoyancy of the flame plume, and may be carried by the wind. Firebrands can be transported for hundreds or even tens of thousands of metres by wind (Hall *et al.* 2015). Spot fire may form continuous showers (Fernandez-Pello 2017), and normally cause numerous new ignitions beyond the primary burning zone (Tarifa *et al.* 1965; Manzello *et al.* 2020). Spot fire plays a significant role in the rapid spread of wildland and wildland–urban interface (WUI) fires (Suzuki *et al.* 2015; Manzello 2020) and poses a severe risk of igniting large areas of wildland fuels and even WUI buildings (Sardoy *et al.* 2007; Song *et al.* 2017; Santoso *et al.* 2019). At least 50% of ignitions are attributable to firebrands in WUI areas (Mell *et al.* 2010; Fang *et al.* 2021).

During the past several decades, there has been much attention on firebrand generation, transport and ignition (for more details, refer to the comprehensive reviews by Manzello *et al.* (2020) and Wadhvani *et al.* (2022)). Prediction of the flight distance and trajectory of self-sustained burning firebrands highly depends on understanding firebrand burning. However, despite considerable research on firebrand transport, the firebrand burning mechanism under wind (forced convection) is still poorly understood. Most relevant studies fall into empirical modelling or experimental analysis. Tarifa *et al.* (1965) pioneered wind tunnel experiments on spherical and cylindrical firebrand transport and developed empirical models to discuss the influence of firebrand size, density, type and moisture on transport trajectories. Some studies investigated the trajectories of firebrands initially elevated from fire plumes by theoretical calculations (Lee and Hellman 1969; Woycheese *et al.* 1999) or numerical simulations (Anthenien *et al.*

2006; Oliveira *et al.* 2014). Albin 1983 developed an empirical burning rate model for transporting firebrands in wind-driven fires by line thermals. Himoto and Tanaka (2005) proposed a model for wind-driven firebrands without considering firebrand burning. Ellis (2013) measured the duration of flaming burning (flameout time), total burning time during flight (burnout time) and mass at burnout of 192 samples in a CSIRO blower-type vertical wind tunnel (Knight 2001). However, the burning mechanism of firebrands was not discussed. Almeida *et al.* (2011) also established an empirical mass model for flaming and smouldering firebrands with a vertical wind tunnel at different speeds.

Very limited research has touched on the firebrand burning mechanism under forced convection through experimental and theoretical analyses. Mukunda *et al.* (1985) conducted burning experiments on wooden spheres under natural convection and developed a wood burning model, showing mass loss and diameter reduction with increasing initial diameter of firebrand samples. They predicted the burning time, mass, diameter, surface temperature and core temperature of firebrands. Song *et al.* (2017) analysed the flight distance and mass change of firebrands experimentally. However, firebrand burning was not fully self-sustaining, and the experimental transport range was limited. Urban *et al.* (2019a) provided a method to measure the surface temperature of firebrands, but did not correlate the surface temperature with the firebrand burning rate.

Moreover, firebrands under forced convection may be in a mode of flaming or smouldering burning. However, burning modes have rarely been distinguished in evaluating firebrand burning rate and size. During firebrand burning, the pyrolysis front propagates inward and forms char gradually. When wood pyrolysis is complete, the inhibitory effect of pyrolysis gas on oxygen diffusion is weakened, allowing more oxygen to diffuse to the firebrand surface. As firebrand temperature increases, char oxidation occurs (Sardoy *et al.* 2006) on the surface rather than through the whole sample (Sardoy *et al.* 2007). Tse and Fernandez-Pello (1998) suggested that volume reduction may be attributed to char oxidation on the particle surface. Based on liquid fuel burning theory (Spalding 1953; Turns 2000), the mass transfer number B is an important parameter affecting the burning rate of firebrands (Pagni 1981; Turns 2000; Lattimer *et al.* 2022). Woycheese and Pagni (1999) determined the maximum propagation distance of combusting firebrands exposed to the fire plume and constant horizontal wind, without considering the mode of flaming or smouldering burning. Lattimer *et al.* (2022) used analytical equations to evaluate firebrand temperature, mass loss rate, char diameter and burning duration based on char oxidation. However, wood pyrolysis was neglected.

Considering the above problems, this work studies the flaming and smouldering burning of wood firebrands under forced convection by experimental and modelling approaches. Firebrand density, burning rate, projected area and surface temperature are analysed. Correlations

for firebrand burning characteristics are developed and used in a firebrand transport model.

Experimental methods

Sample

Reflective of the firebrand shape and size observed in WUI fires and typically used in experimental studies (Xiong *et al.* 2020; Manzello *et al.* 2020), spherical wooden firebrands (*Schima Superba*) with diameters of 10, 15, 20 and 25 mm were used as the samples in the present work. The sphere has been regarded as a typical shape for firebrand research (Wadhvani *et al.* 2022; Dal-Ri dos Santos and Yaghoobian 2023) because natural firebrands sometimes undergo a gradual transition into near-spheroids through burning (Urban *et al.* 2019b). Moreover, the burning model and transport model for spherical wooden firebrands can be extended for cylinder firebrands by simple geometric transformation (Lattimer *et al.* 2022). Before the experiments, the samples were dried in a drying oven (Jinghong electric heating blast drying oven, XMTD-8222) at 100–120°C for 24 h (Mukunda *et al.* 1985) and were then stored in a sealed bag. After drying, the moisture contents of the samples were 0.73–1.56%. The densities of the oven-dry samples were 0.520–0.599 g cm⁻³. The sample masses were 0.267–4.705 g, with a relative standard deviation <5%.

Experiment

The experimental set-up is illustrated in Fig. 1. A jet fan (Suitai, China, model SDS4.0-2.2kw-2p), equipped with two layers of damping nets inside the outlet end, provided a stable airflow. The wind speed was adjusted through a frequency converter. A hot-wire anemometer (Kanomax, CTA/HWA7000) was placed 5 cm above the centreline of the firebrand to measure the wind speed. The wind speeds varied between 0 and 8 m s⁻¹ with a fluctuation of ±5%. A digital video camera (Sony FDR-AX60, 50 frames s⁻¹, 1920 × 1080 pixels) and an infrared thermal imaging camera (American FLIR T650sc, 30 frames s⁻¹, 640 × 480 pixels) recorded firebrand burning and surface temperature from the front view. Firebrands were ignited by a propane igniter, which was turned off immediately when the firebrands reached self-sustaining burning. Self-sustaining burning means that after the igniter is removed, the firebrand continues to burn until firebrand breakage occurs. Under the same experimental conditions, the ignition times are identical. Burned mass was measured with an electronic balance (Jingfei Instrument Technology, DHS-10A, resolution 0.005 g) after the sample was quenched with water and then dried. As a stationary firebrand burns fast on the windward side and slowly on the leeward side, the firebrand in each test of this work was rotated on a fixing nail at a speed of 5 s per circle for uniform burning.

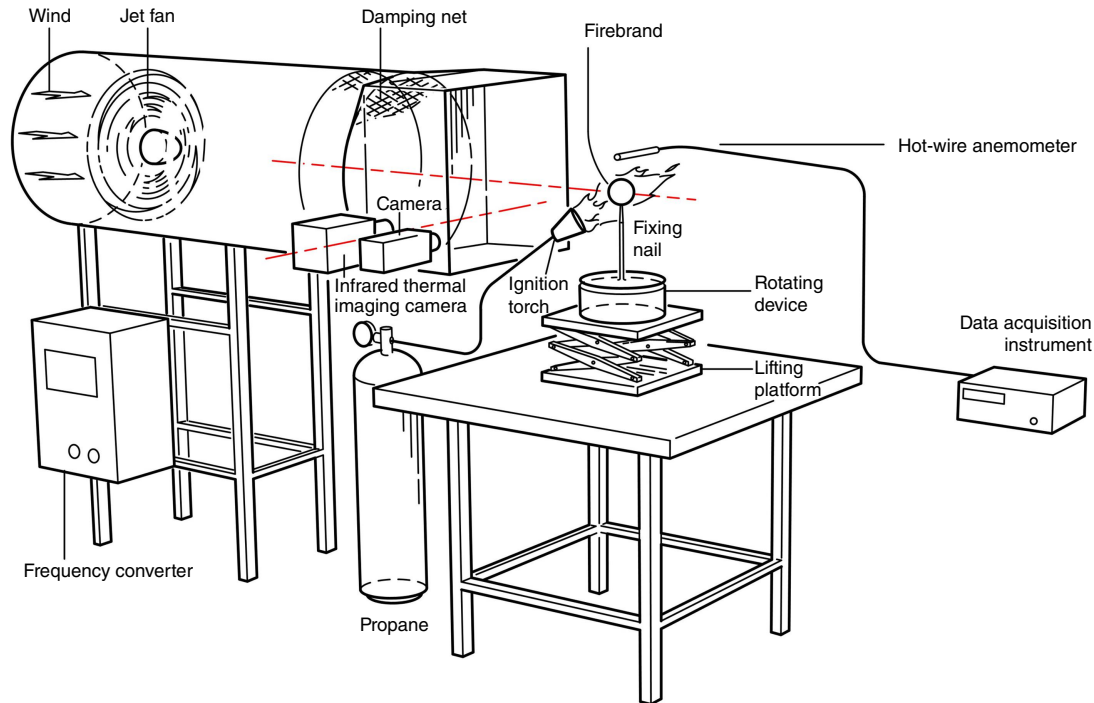


Fig. 1. Experimental setup for firebrand burning under forced convection.

The rotating samples under forced convection are close to the conditions of natural firebrands under wind (Manzello *et al.* 2020). Burning tests of rotational and non-rotational firebrands under natural convection showed comparable temporal variations of firebrand masses. Therefore, the speed relative to air caused by rotating (calculated to be lower than 0.0126 m s^{-1}) is ignored in this work.

We quenched the firebrand for each set of experimental conditions at approximately 20 different moments and measured the instantaneous features such as sample mass and projected area. The quenched firebrands were dried to a moisture content of 2.21–3.76%. For each set of experimental conditions, a large number of repeated tests were performed before the experiment to obtain the burning duration of firebrands. Then, the entire burning duration was divided into ~ 20 instants for firebrand quenching. This step is consistent with Mukunda *et al.* (1985). The electronic balance was utilised for larger firebrand masses ($> 12.95 \text{ g}$ (Almeida *et al.* 2011)) or lower wind speeds ($< 2 \text{ m s}^{-1}$ (Lattimer *et al.* 2022)) without quenching the firebrand. However, the sample masses ($< 4.70 \text{ g}$) and wind speeds ($> 2 \text{ m s}^{-1}$) in the present study, in accord with those of firebrands in natural fires (Hall *et al.* 2015; Storey *et al.* 2020b), caused unacceptable fluctuation in pre-experiments without quenching. The firebrand surface temperature was measured by an infrared thermal imaging camera, calibrated using a thermocouple contacting the surface of non-rotating firebrands. An emissivity of 0.9 (Sardoy *et al.* 2007; Lattimer *et al.* 2022) was adopted for the same temperature as the thermocouple. The firebrand image recorded

by a digital video camera was converted to a greyscale image and then into a binary image by setting a cut-off threshold. The projected area of the firebrand was calculated with pixels and a reference scale, and then the firebrand diameter was obtained. Each experiment was repeated at least four times.

Model description

At low wind speeds, the firebrand is first flaming and then smouldering. At high wind speeds, the firebrand is always smouldering. The mass and volume of a firebrand during burning decrease with burning time. At low wind speeds, the firebrand density decreases monotonically with burning time during flaming, whereas it does not change significantly during smouldering.

Flaming and smouldering firebrands involve different char oxidation mechanisms, with the main products being CO and CO₂. The firebrands in this work are assumed to be homogeneous wood. A mechanism of firebrand burning (consisting of wood pyrolysis and char oxidation) is proposed, and the ratio of wood pyrolysis rate to char oxidation rate is determined. A burning rate model incorporating the wood pyrolysis rate, char oxidation rate and a convective term is developed. Based on mass conservation, the reduction rate of the firebrand projected area is evaluated from the char oxidation rate under forced convection. The firebrand surface temperature is derived in terms of condensed-phase energy conservation. The surface temperature of the firebrand is mainly determined by radiation, and the

relationship between surface temperature and wind speed is then obtained. Finally, based on the above, and in combination with the principles of mechanics, a firebrand transport model is developed to calculate the transport trajectory and essential parameters affecting the burning of firebrands.

Results and discussion

Experimental observations

Fig. 2 shows the burning phenomena of a firebrand with a diameter of 20 mm under different wind speeds. The dotted white lines denote the specific position of the fixing nail. For each wind speed, the first image corresponds to the moment when the propane igniter was just turned off, and the last image of the smouldering stage corresponds to firebrand breakage. As observed, the firebrands first burned with a flame, and after the flame was extinguished, residue smouldering continued at wind speeds of 2 and 4 m s⁻¹. The flame was extinguished quickly and then residue smouldering continued at wind speeds of 6 and 8 m s⁻¹.

The firebrand burning results in a reduction in mass and size, as well as eventual breakage along the wood grain. The firebrand breaks off and forms multiple smaller firebrands that are blown away by the wind. The higher the wind speed, the shorter the firebrand breakage time. The breakage of the firebrand significantly promotes mass and heat transfer and reduces the firebrand mass. Although firebrand burning was suggested to be affected by firebrand breakage

(Thunman *et al.* 2002; Kuo and Hwang 2003; Almeida *et al.* 2011) and ash formation (Hall *et al.* 2015), we do not consider these effects in this work because firebrand breakage occurred only in the last few seconds and the ash accumulated only at the wind speed of 2 m s⁻¹ during char oxidation. Additionally, the thin ash layer (Fig. 2) is considered to have a minor effect on surface energy transfer and gas diffusion (Wong *et al.* 2022).

Firebrand density and burning mechanism

The temporal variation of firebrand density under different wind speeds and particle diameters is shown in Fig. 3. In Fig. 3a, under wind speeds of 2 and 4 m s⁻¹, Regimes I–III correspond to the flaming stage, flame extinction and the smouldering stage, respectively. The dotted lines denote the time of flame extinction.

Mukunda *et al.* (1985) carried out a combustion experiment on spheroid wood particles with different diameters under natural convection. Experimental results showed that the diameter squared decreases by 20–25%, and the particle mass decreases by 75–80% during flaming. The mass loss of a firebrand is caused by pyrolysis and char oxidation, while the volume loss is mainly attributable to char oxidation (Tse and Fernandez-Pello 1998; Porteiro *et al.* 2007). The firebrand density decreases in flaming (Regime I) owing to wood pyrolysis and char oxidation. The firebrand density almost remains constant in smouldering (Regime III), in which char oxidation is the primary reaction. Char oxidation can exist with flaming here because the flame cannot fully

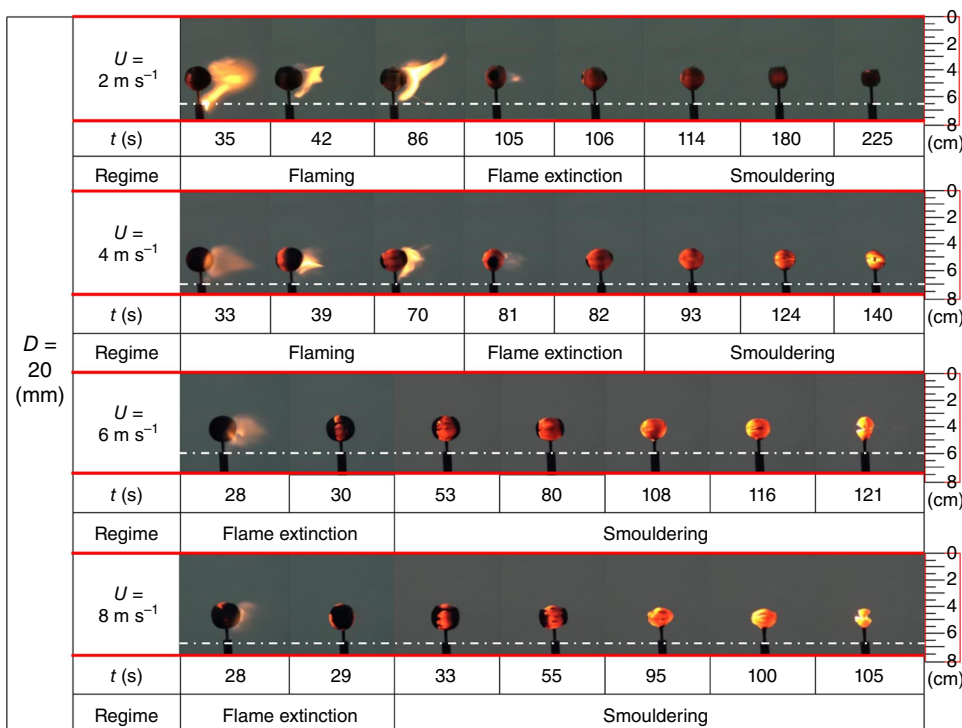


Fig. 2. Firebrand burning under different wind speeds.

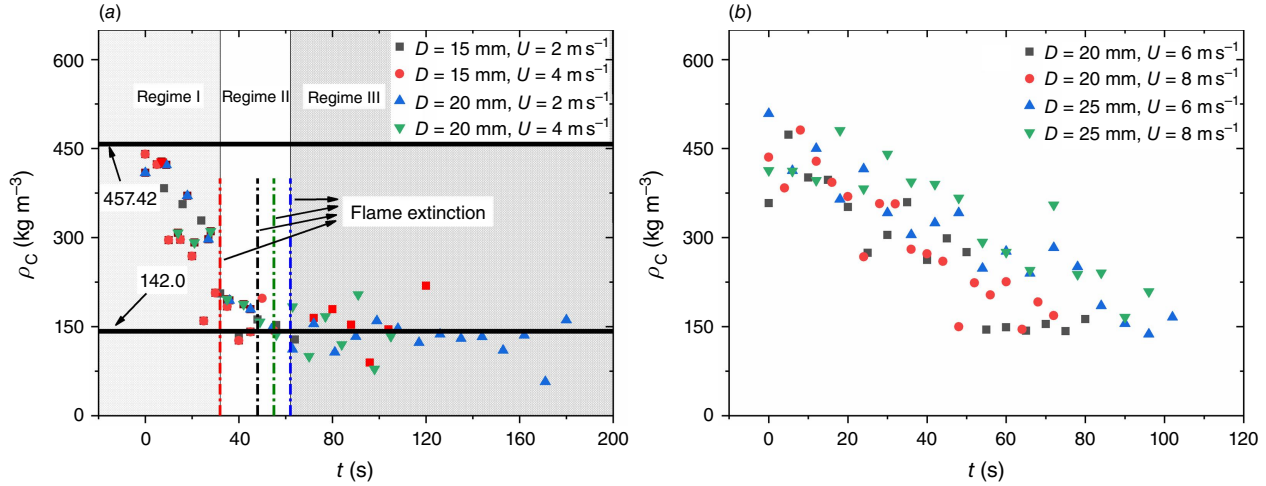
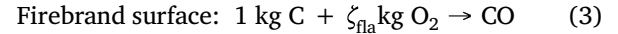
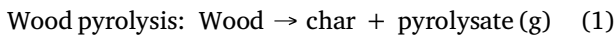


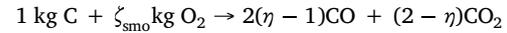
Fig. 3. Firebrand density under (a) 2 and 4 m s⁻¹, (b) 6 and 8 m s⁻¹ wind speeds.

cover the firebrand surface. Thus, the reduction in firebrand density is considered mainly attributable to wood pyrolysis. Pyrolysis and char oxidation occur simultaneously during flaming. The squared diameter loss is ~25%, density loss is ~70%, and mass loss is ~80%, of which pyrolysis accounts for ~69%. The experimental results are consistent with those of Mukunda *et al.* (1985). In Fig. 3b, smouldering firebrand density decreases under wind speeds of 6 and 8 m s⁻¹, which differs from the almost constant firebrand density in the smouldering stage under 2 and 4 m s⁻¹ (Regime III in Fig. 3a). This difference may be attributable to the fact that the smouldering firebrand under lower wind speeds is dominated by char oxidation, and under higher wind speeds, undergoes pyrolysis and char oxidation simultaneously.

The volatiles released from wood pyrolysis support flaming combustion. Wood char normally contains small amounts of oxygen, hydrogen and nitrogen, which can be neglected. Thus, char is assumed to be made of pure carbon (Porteiro *et al.* 2007). The flame then affects the char oxidation reaction. Porteiro *et al.* (2007) assumed that char oxidation occurring in flaming and smouldering firebrands results in the simultaneous generation of CO and CO₂. However, the oxygen diffuses to the firebrand surface with difficulty in flaming burning, whereas it directly contacts the char surface in smouldering burning. Thus, for a flaming firebrand, CO₂ and CO are generated on the flame and firebrand surfaces, respectively (Caram and Amundson 1977). For a smouldering firebrand, CO and CO₂ are produced on the firebrand surface, and the overall rate of char consumption is calculated using Eqn 4 as the ratio between CO and CO₂ (Porteiro *et al.* 2007). The above considerations lead to the following firebrand burning mechanism:



Firebrand surface:



$$\eta = 2[1 + 4.3\exp(-3390/T)]/[2 + 4.3\exp(-3390/T)] \quad (4)$$

where ζ is the stoichiometric coefficient, and η is the CO-to-CO₂ ratio. The subscripts fla and smo denote flaming and smouldering stages, respectively. The temperature T (K) is 950–1150 K, and the corresponding η is 1.057–1.101. The $\eta = 1.078$ for a temperature of 1050 K is chosen, and the resulting error is negligible. $\zeta_{\text{fla}} = 1.333$, and $\zeta_{\text{smo}} = 2.474$. For wind speeds of 2 and 4 m s⁻¹, the flaming stages follow Eqns 1–3, and the smouldering stages follow Eqn 4. For wind speeds of 6 and 8 m s⁻¹, the flaming stages are ignored, and the smouldering stages follow Eqns 1 and 4.

Burning rate

The burning rate (mass loss rate) of a firebrand is

$$\frac{dm_{\text{fb}}}{dt} = -(1 + \varphi_{\text{pyr}})m'_{\text{char}} \quad (5)$$

where m_{fb} is the firebrand mass (g), t the burning time (s), m'_{char} the char oxidation rate (g s⁻¹), φ_{pyr} the ratio of wood pyrolysis rate to char oxidation rate, and the subscript pyr denotes wood pyrolysis.

For the flaming stages at 2 and 4 m s⁻¹:

$$m_{\text{pyr}} = \rho_{\text{fla},0} \Omega_{\text{fla},0} - \rho_{\text{fla},\text{fe}} \Omega_{\text{fla},0} \quad (6)$$

$$m_{\text{oxi}} = (\rho_{\text{fla},0} \Omega_{\text{fla},0} - \rho_{\text{fla},\text{fe}} \Omega_{\text{fla},\text{fe}}) - m_{\text{pyr}} = \rho_{\text{fla},\text{fe}} \Omega_{\text{fla},0} - \rho_{\text{fla},\text{fe}} \Omega_{\text{fla},\text{fe}} \quad (7)$$

$$\overline{\varphi}_{\text{pyr}} \equiv \frac{m_{\text{pyr}}}{m_{\text{oxi}}} = \frac{\rho_{\text{fla},0}\Omega_{\text{fla},0} - \rho_{\text{fla,fe}}\Omega_{\text{fla},0}}{\rho_{\text{fla,fe}}\Omega_{\text{fla},0} - \rho_{\text{fla,fe}}\Omega_{\text{fla,fe}}} \quad (8)$$

where $\overline{\varphi}_{\text{pyr}}$ is the mean ratio of wood pyrolysis rate to char oxidation rate in the burning stage, Ω the firebrand volume (m^3), ρ the firebrand density (kg m^{-3}). The subscript *oxi* denotes the char oxidation, 0 the initial value, and *fe* the flame extinction.

For the smouldering stages at 2 and 4 m s^{-1} :

$$\overline{\varphi}_{\text{pyr}} = 0 \quad (9)$$

For the smouldering stages at 6 and 8 m s^{-1} :

$$m_{\text{pyr}} = \rho_{\text{smo},0}\Omega_{\text{smo},0} - \rho_{\text{bre}}\Omega_{\text{smo},0} \quad (10)$$

$$m_{\text{oxi}} = \rho_{\text{smo},0}\Omega_{\text{smo},0} - \rho_{\text{bre}}\Omega_{\text{bre}} - (\rho_{\text{smo},0}\Omega_{\text{smo},0} - \rho_{\text{bre}}\Omega_{\text{smo},0}) = \rho_{\text{bre}}\Omega_{\text{smo},0} - \rho_{\text{bre}}\Omega_{\text{bre}} \quad (11)$$

$$\overline{\varphi}_{\text{pyr}} = \frac{\rho_{\text{smo},0}\Omega_{\text{smo},0} - \rho_{\text{bre}}\Omega_{\text{smo},0}}{\rho_{\text{bre}}\Omega_{\text{smo},0} - \rho_{\text{bre}}\Omega_{\text{bre}}} \quad (12)$$

where the subscript *bre* denotes firebrand breakage. Table 1 presents firebrand density (ρ) and volume (Ω), where D is firebrand diameter (mm), and U is the wind speed (m s^{-1}). The $\overline{\varphi}_{\text{pyr}}$ value is 4.51 for the flaming stages at 2 and 4 m s^{-1} and the smouldering stages at 6 and 8 m s^{-1} , indicating mass loss due to wood pyrolysis is much greater than that caused by char oxidation, consistent with Zhu and Liu (2020).

The sample in this work is assumed to be homogeneous wood with uniform mass loss. The gas diffusivity D_m under air is $1.6 \times 10^{-5} \text{m}^2 \text{s}^{-1}$ for CO_2 at 298 K and $2.08 \times 10^{-5} \text{m}^2 \text{s}^{-1}$ for CO at 293 K. Thermal diffusion α is $2.058 \times 10^{-5} \text{m}^2 \text{s}^{-1}$ for air at 300 K. Thus, the Lewis number $\text{Le} = \alpha/D_m \approx 1$ (Turns 2000; Lattimer *et al.* 2022). The power law relationship between the Nusselt (Nu) and Reynolds (Re) numbers has been fully studied for external flow (Incropera *et al.* 2007). They are correlated by a multiplicative correction of an additional convective term under

forced convection for droplet combustion (Faeth 1977; Incropera *et al.* 2007):

$$\text{Nu} = 2 + 0.6\text{Re}^{1/2}\text{Pr}^{1/3} \quad (13)$$

where the Prandtl number $\text{Pr} = 0.707$ (Incropera *et al.* 2007; Lattimer *et al.* 2022). As the Pr value varies from 0.707 to 0.728 within 300–1200 K (Incropera *et al.* 2007; Lattimer *et al.* 2022), the temperature-induced error is within 3%. $\text{Re} = D_0\rho_g U/\mu$ (Lattimer *et al.* 2022), where D_0 is the initial firebrand diameter (mm), and the dynamic viscosity $\mu = 1.846 \times 10^{-5} \text{N s m}^{-2}$ (Incropera *et al.* 2007). The diameter-induced mean error in $\text{Re}^{1/2}$ is $\sim 5.5\%$.

Based on the char oxidation rate ($m'_{\text{char}} = 2\pi r\rho_g D_m \text{Nu} \ln(1+B)L/D$, L is firebrand length (mm)) (Lattimer *et al.* 2022), the burning rate of spherical wooden firebrands under forced convection is formulated as

$$m'_{\text{fb}} = 2\pi D\rho_g D_m \ln(1+B)(1 + \overline{\varphi}_{\text{pyr}}) \times [1 + \text{fb}(\text{Re}^{1/2}\text{Pr}^{1/3})/2] \quad (14)$$

where the gas diffusion constant $D_m = 1.84 \times 10^{-5} \text{m}^2 \text{s}^{-1}$ (Lattimer *et al.* 2022), and the air density $\rho_g = 1.1614 \text{kg m}^{-3}$ at 300 K (Incropera *et al.* 2007). The mass transfer number $B_{\text{smo}} = Y_{\text{O}_2,\infty}/\zeta_{\text{smo}}$ and $B_{\text{fla}} = Y_{\text{O}_2,\infty}/\zeta_{\text{fla}}$, where Y is the mass fraction ($Y_{\text{O}_2,\infty} = 0.233$ and $Y_{\text{O}_2,s} \approx 0$). The firebrand diameter D (see Fig. 4) is obtained by linear fitting (Tarifa *et al.* 1965).

$$D^2 = D_0^2 - (\beta_D + \delta_D U)t \quad (15)$$

Here, the parameters β_D and δ_D depend on wood type and moisture content.

$$\frac{dS}{dt} = -(\beta + \delta U) \quad (16)$$

where S is the projected area of the sample (mm^2), and the parameters $\beta = \beta_D\pi/4$ and $\delta = \delta_D\pi/4$. Thus, the burning rate

Table 1. Density (ρ) and volume (Ω) for firebrand burning.

D (mm)	U (m s^{-1})	$\Omega \times 10^{-7}$ (m^3)				ρ^A (kg m^{-3})			
		$\Omega_{\text{fla},0}$	$\Omega_{\text{fla,fe}}$	$\Omega_{\text{smo},0}$	Ω_{bre}	$\rho_{\text{fla},0}$	$\rho_{\text{fla,fe}}$	$\rho_{\text{smo},0}$	ρ_{bre}
15	2	14.3	7.0	8.7	7.0	457.4	142.0	142.0	142.0
15	4	13.6	7.1	8.8	5.8	457.4	142.0	142.0	142.0
20	2	34.0	19.8	22.8	6.0	457.4	142.0	142.0	142.0
20	4	37.2	17.3	20.1	7.2	457.4	142.0	142.0	142.0
20	6	–	–	36.9	17.7	–	–	457.4	142.0
20	8	–	–	38.5	17.1	–	–	457.4	142.0
25	6	–	–	73.3	37.5	–	–	457.4	142.0
25	8	–	–	73.1	38.9	–	–	457.4	142.0

^A ρ is calculated by dividing m_{fb} by Ω in each single test.

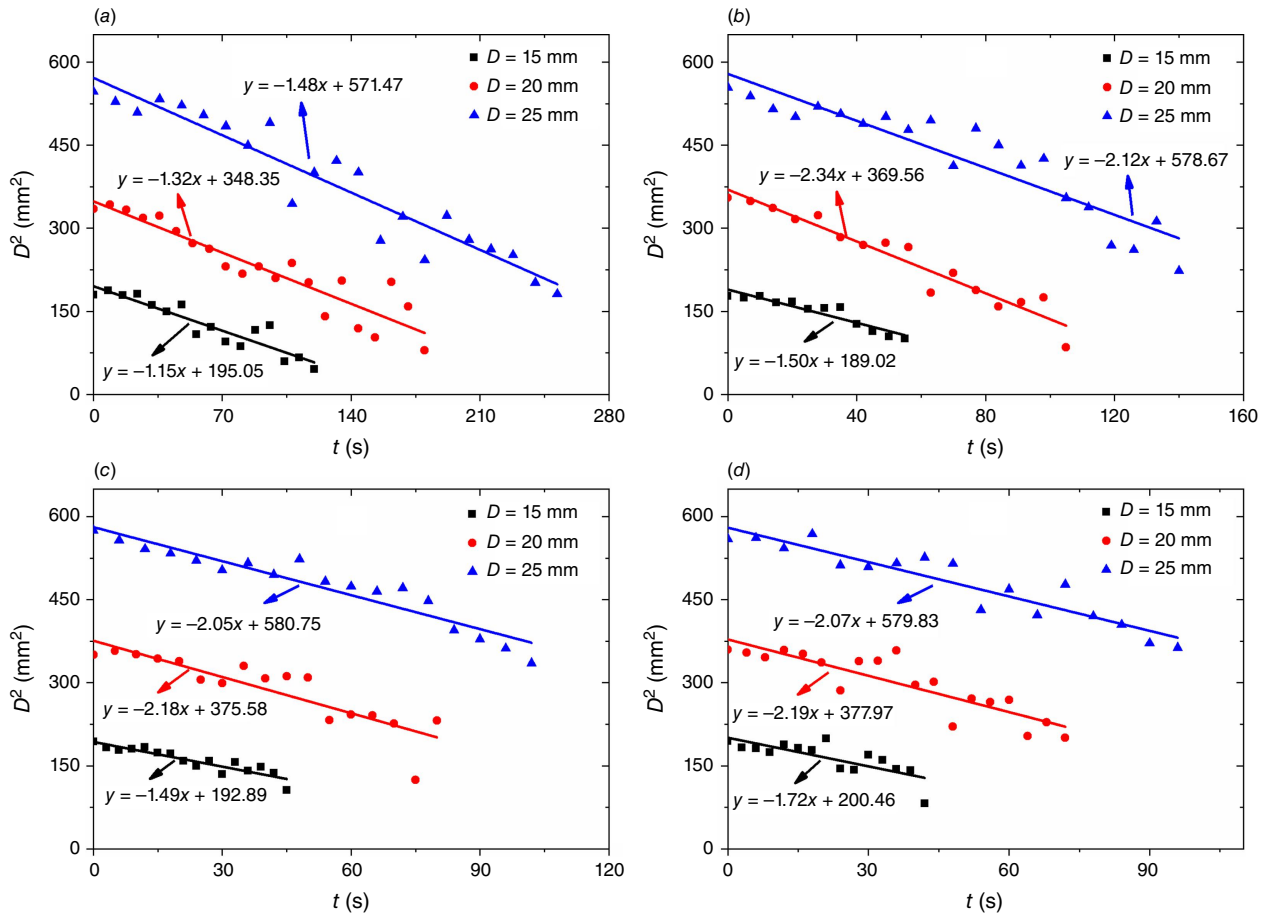


Fig. 4. Firebrand diameter change under (a) 2 m s^{-1} , (b) 4 m s^{-1} , (c) 6 m s^{-1} , and (d) 8 m s^{-1} wind speeds.

depends on firebrand diameter, flaming or smouldering burning, pyrolysis rate and relative wind speed.

Then, only parameter fb is unknown in Eqn 14. The firebrand mass (Fig. 5) is introduced to solve for fb , and expressed as:

$$m_{fb} = m_0 - \int_0^t m'_{fb} dt \quad (17)$$

where $m_0 = \Omega_{fla,0} \rho_{fla,0}$ or $m_0 = \Omega_{smo,0} \rho_{smo,0}$ (Table 1). We substitute Eqn 14 (combined with Eqn 15) into Eqn 17, and integrate the expression. Then, the correction factor fb value (Fig. 6) is determined by non-linear fitting Eqn 17 in integral form with $\overline{\varphi}_{pyr} = 4.51$ and different experimental m_{fb} , m_0 and D_0 values. The trends of burned mass with quenching over burning time agree well with previous reports (Almeida *et al.* 2011; Lattimer *et al.* 2022) at wind speeds of 2 and 4 m s^{-1} . Spherical wooden firebrand burning, involving wood pyrolysis and char oxidation, significantly differs from droplet combustion in heat and mass transfer processes. Thus, the fb values for flaming and smouldering burning of wood firebrands obtained by the above regression analysis, rather than the empirical value of 0.6 concerning droplet combustion, are used for the following calculations.

Projected area

The variation of firebrand projected area is mainly attributable to char oxidation (Tse and Fernandez-Pello 1998; Porteiro *et al.* 2007). The char oxidation rate is:

$$\frac{dm_{char}}{dt} = -m'_{char} \quad (18)$$

The char mass is formulated as:

$$m_{char} = \rho_{char} \Omega = \rho_{char} \pi D^3 / 6 \quad (19)$$

Based on the char oxidation rate ($m'_{char} = 2\pi D \rho_g D_m \ln(1 + B) [1 + fb(\text{Re}^{1/2} \text{Pr}^{1/3})/2]$) from Eqns 14, 18, and 19, the reduction rate of the projected firebrand is:

$$\frac{dS}{dt} = -\frac{2\pi \rho_g D_m}{\rho_{char}} \ln(1 + B) \times \left[1 + \frac{fb(\text{Re}^{1/2} \text{Pr}^{1/3})}{2} \right] \quad (20)$$

The theoretical dS/dt values for flaming and smouldering firebrands are indicated in Fig. 7, and agree with the experimental data. Based on Eqn 20,

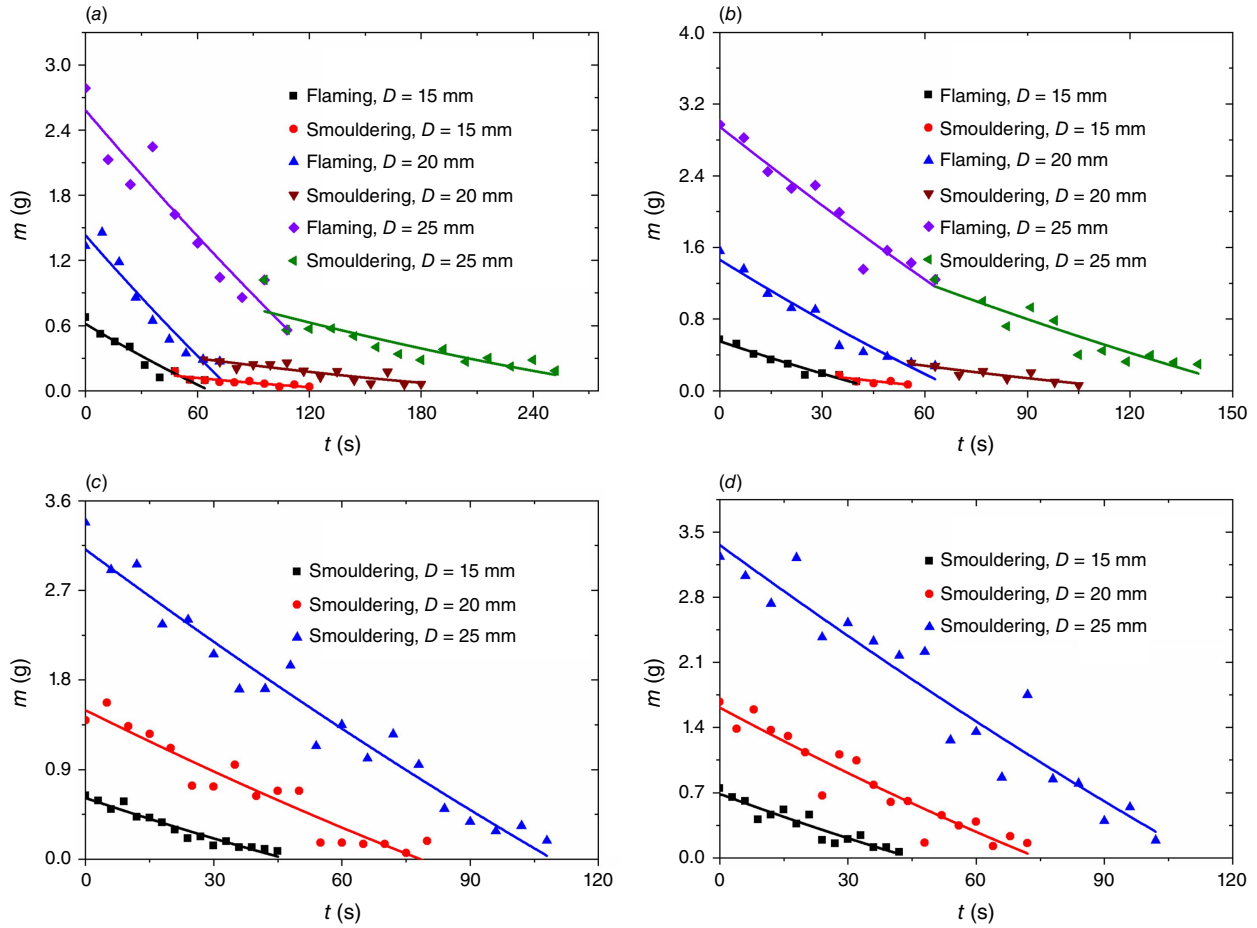


Fig. 5. Firebrand mass change under (a) 2 m s⁻¹, (b) 4 m s⁻¹, (c) 6 m s⁻¹, and (d) 8 m s⁻¹.

$$\frac{dS}{dt} = -f \left(\rho_{\text{char}}^{-1}, \ln(1 + B), \left[1 + \frac{\text{fb}(D_0^{1/2} \rho_g^{1/2} \text{Pr}^{1/3})}{2\mu^{1/2}} U^{1/2} \right] \right) \quad (21)$$

A higher dS/dt value corresponds to a higher char density, a lower $\ln(1 + B)$, a lower firebrand diameter, or a lower wind speed. The $\ln(1 + B)$ value in flaming is much higher than that in smouldering. Thus, dS/dt in flaming is slightly lower than in smouldering under 2 and 4 m s⁻¹ wind speeds in Fig. 7.

Surface temperature

Fig. 8 shows the experimental firebrand surface temperature (extracted as the average value in the first 10 s) under forced convection. The higher the wind speed, the higher the surface temperature, indicating that the heat generated by firebrand burning exceeds the heat loss when the wind speed is increased. As presented in Fig. 9, the condensed-phase energy conservation at the firebrand surface is:

$$\alpha_f^{\text{char}} m'_{\text{fb}} \Delta h_{\text{char}} = -k_{\text{sol}} 4\pi r_s^2 \frac{dT}{dr} \Big|_{r_s} + h_{\text{conv}} 4\pi r_s^2 (T_s - T_{\text{film}}) + \epsilon_s 4\pi r_s^2 \sigma (T_s^4 - T_{\infty}^4) \quad (22)$$

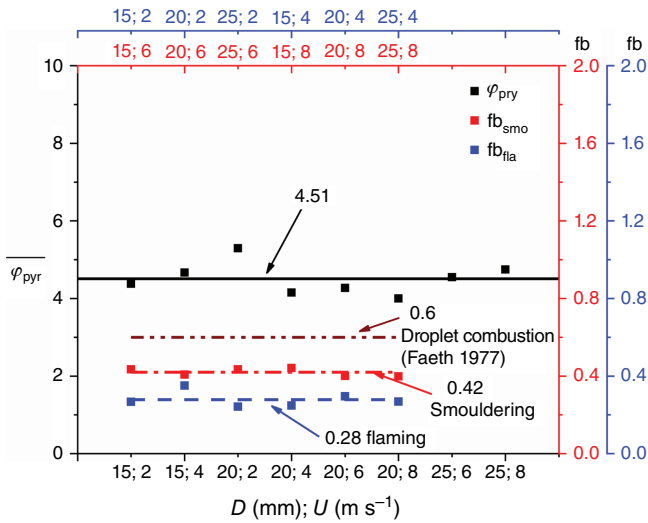


Fig. 6. Ratio of wood pyrolysis rate to char oxidation rate ($\overline{\varphi}_{\text{pyr}}$) and flow parameters (fb).

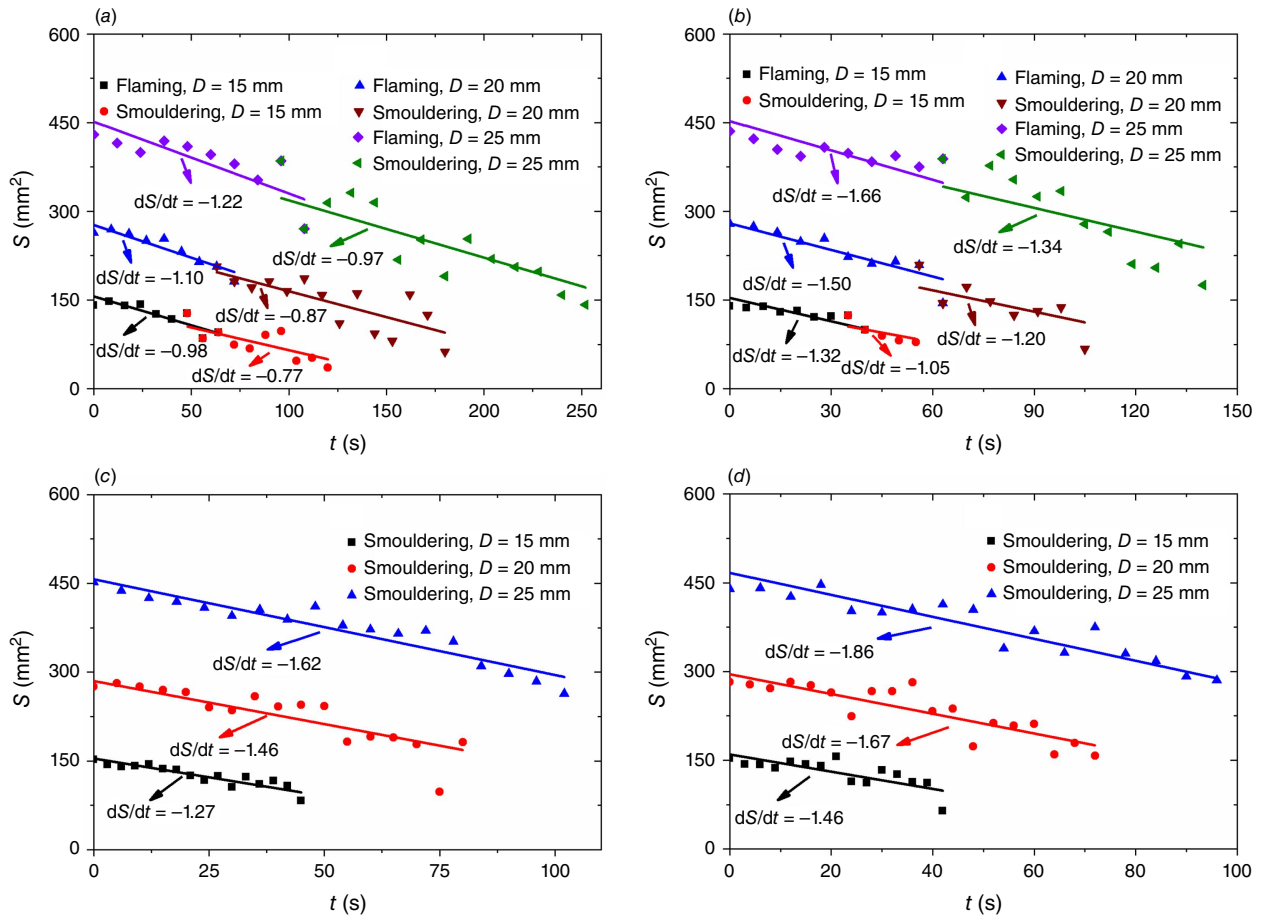


Fig. 7. Theoretical and experimental dS/dt values at wind speeds of (a) 2 m s^{-1} , (b) 4 m s^{-1} , (c) 6 m s^{-1} , and (d) 8 m s^{-1} .

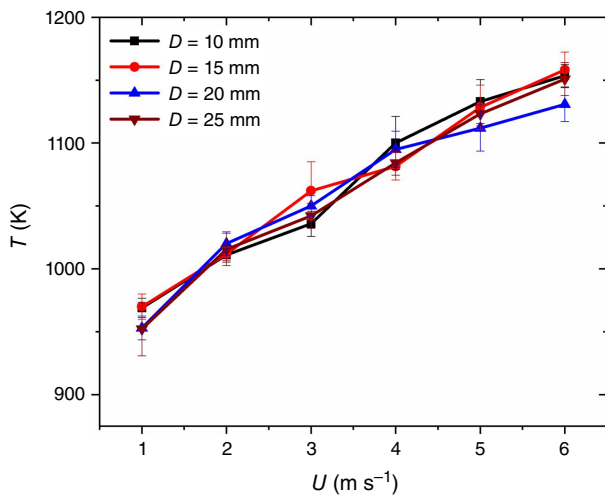


Fig. 8. Relationship between surface temperature and wind speed.

where T_s denotes the firebrand surface temperature, the mass fraction of char in firebrand $\alpha_{fb}^{char} = 0.182$ ($\overline{\varphi}_{pyr} \approx 4.51$), the heat of char oxidation Δh_{char} is 21.0 MJ kg^{-1} (Lattimer et al. 2022), and the thermal

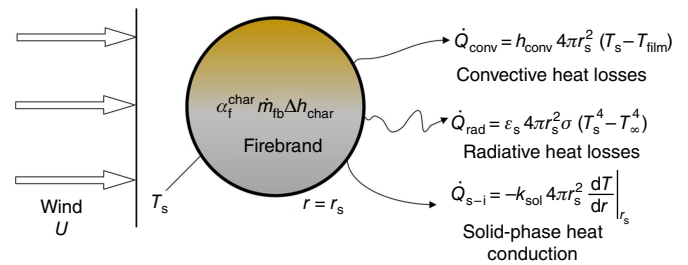


Fig. 9. Energy fluxes on the firebrand surface.

conductivity of the solid phase k_{sol} is $0.1 \text{ W m}^{-1} \text{ K}^{-1}$ (Sardoy et al. 2006). The firebrand radius $r = D/2$ and the subscript s denotes the surface. The temperature of the gas phase film $T_{film} = (T_s + T_\infty)/2 \approx 700 \text{ K}$. The convective heat transfer coefficient $h_{conv} = \text{Nu} k_{film}/D$, where the thermal conductivity of air k_{film} is $5.24 \times 10^{-2} \text{ W m}^{-1} \text{ K}^{-1}$ at 700 K . The Stefan-Boltzmann constant is $\sigma = 5.67 \times 10^{-8} \text{ W m}^{-2} \text{ K}^{-4}$. The temperature $T_\infty = 293.15 \text{ K}$. The emissivity $\epsilon_s = 0.9$ (Sardoy et al. 2007; Lattimer et al. 2022). It is reasonable to assume that the emissivity remains constant because the temperature values are measured in the first 10 s, during which the firebrand surface is always

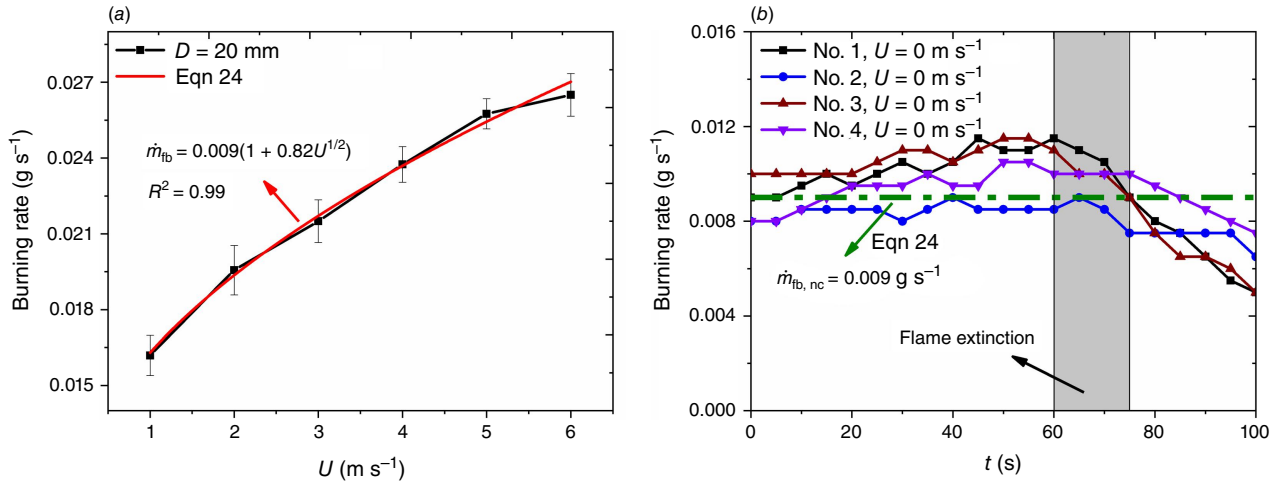


Fig. 10. Burning rate of firebrands under (a) forced convection and (b) natural convection ($D = 20$ mm).

covered with char (Fig. 2). The temperature gradient at the firebrand surface (Turns 2000) is

$$\left. \frac{dT}{dr} \right|_{r_s} = \frac{c_p m'_{char,nc} (T_\infty - T_s) \exp(-c_p m'_{char,nc} / 4\pi k_{sol} r_s)}{4\pi k_{sol} r_s^2 [1 - \exp(-c_p m'_{char,nc} / 4\pi k_{sol} r_s)]} \quad (23)$$

where the subscript nc denotes natural convection, and the specific heat capacity at constant pressure c_p is 1075 J kg⁻¹ K⁻¹. The particle diameter varies insignificantly in 10 s and is assumed as a constant D_0 . Then, based on Eqn 14, $m'_{fb,nc}$ satisfies

$$m'_{fb} = f \left[D, \ln(1 + B), \left(1 + \frac{1}{\overline{\varphi}_{pyr}} \right), \left[1 + \frac{fb(D_0^{1/2} \rho_g^{1/2} Pr^{1/3})}{2\mu^{1/2}} U^{1/2} \right] \right] \quad (24)$$

$$= m'_{fb,nc} (1 + K \times U^{1/2})$$

where K is the function coefficient. The larger the firebrand diameter and wind speed, the greater the firebrand burning rate. As illustrated in Fig. 10, the firebrand burning rate significantly depends on the wind speed. The K and $m'_{fb,nc}$ values are obtained by fitting the experimental firebrand burning rate and Eqn 24. The reliability of Eqn 24 is verified by good agreement with experimental data under natural convection. Then, the firebrand surface temperature is calculated with Eqn 22. It is found that the firebrand surface temperature is mainly determined by radiation, with a contribution of more than 90%. $T_s^4 - T_\infty^4 \approx T_s^4$ because $T_s^4 \gg T_\infty^4$. Based on Eqns 22 and 24, the relation between firebrand surface temperature and wind speed is:

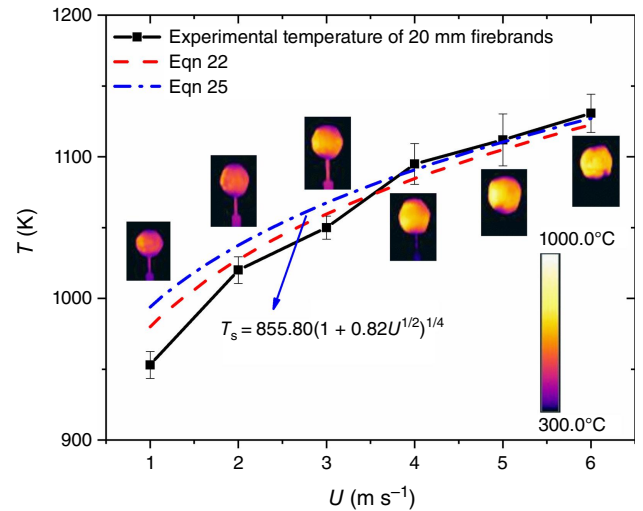


Fig. 11. Relationship between surface temperature and wind speed ($D = 20$ mm).

$$T_s = (\alpha_f^{char} m'_{fb,nc} \Delta h_{char} / \varepsilon_s 4\pi r_s^2 \sigma)^{1/4} (1 + K \times U^{1/2})^{1/4} \quad (25)$$

The experimental and calculated surface temperatures are in good agreement, as shown in Fig. 11. The surface temperature increases with wind speed, as the heat from the firebrand burning overcomes the heat loss.

Transport trajectory

The firebrand trajectory is analysed with some assumptions: (1) firebrand uplift, rotation and vibration are neglected. (2) Firebrands do not affect each other. (3) Only the relative velocity of a firebrand and the surrounding air is considered during the firebrand transport. The firebrand transport model is presented in Fig. 12, where H is the height of the firebrand (m), L_x the horizontal transport distance (m), U_h

the horizontal wind speed ($m s^{-1}$), V_{fb} the firebrand velocity ($m s^{-1}$), F the force (N), $F_{y,G} = mg$ the force exerted by gravity on the firebrand, $F_{y,res}$ the air resistance, V_x the horizontal speed of the firebrand, and V_y the vertical speed of the firebrand. The drag force of wind on the firebrands is equal to the air resistance in the horizontal direction ($F_w = F_{x,res}$). Based on Newton's second law and discretisation technique,

$$\frac{d(m_i \mathbf{V}_{fbi})}{dt} = \rho_{fbi} \Omega_{fbi} \mathbf{g} - \frac{1}{2} \rho_0 C_D S_i \|\mathbf{V}_{fbi} - \mathbf{U}\| (\mathbf{V}_{fbi} - \mathbf{U}) \quad (26)$$

where C_D is the drag coefficient, subscript i denotes iteration and the relative velocity $U_{r,i} \approx \|\mathbf{V}_{fbi} - \mathbf{U}\|$. Based on Eqns 14, 16, 20 and 25, $m'_{fb} = \xi (S_{i-1}^{1/2} + K_{con} \times U_{r,i-1}^{1/2} G_{i-1}^{3/4})$, where $\xi = 4\pi^{1/2} \rho_g D_m \ln(1+B)(1 + \overline{\phi}_{pyr})$, $K_{con} = fb(4/\pi)^{1/4} (Pr \text{ or } Sc)^{1/3} / 2\mu^{1/2}$, $S_i = S_{i-1} - (\beta_{con} + \delta_{con} U_{r,i-1}) \Delta t$, $T_{si} = (\alpha_f^{char} m'_{fb} \Delta h_{char} / \varepsilon_s 4\pi r_{si}^2 \sigma)^{1/4}$, $m_i = m_{i-1} - m'_{fb} \Delta t$, and Δt is the time step.

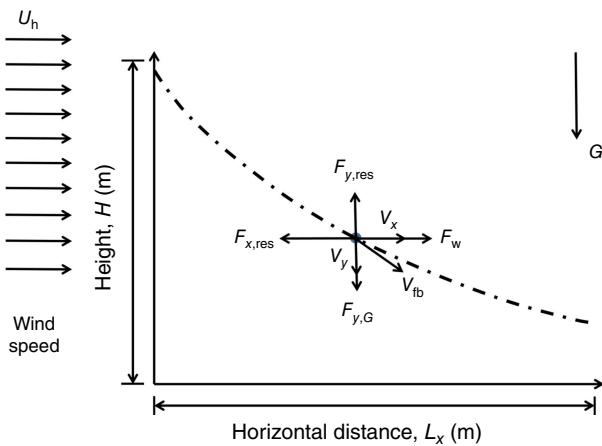


Fig. 12. Firebrand transport model.

The height of firebrand and horizontal flight distance are:

$$H = H_{max} - \sum_{i=1}^n (V_{y,i} \Delta t), L_x = \sum_{i=1}^n (V_{x,i} \Delta t) \quad (27)$$

The drag coefficient (Ganser 1993) is calculated by:

$$C_D = \frac{24}{Re K_1} [1 + 0.1118 (Re K_1 K_2)^{0.6567}] + \frac{0.4305 K_2}{1 + 3305 / (Re K_1 K_2)} \quad (28)$$

where K_1 is Stokes' shape factor, and K_2 is Newton's shape factor. Here, $K_1 = K_2 = 1$. The transport trajectory is calculated for firebrands of $D = 15, 20$ and 25 mm in self-sustaining burning. The initial values of the mass (Eqn 17, Fig. 5) and the projected area (Eqn 20, Fig. 7) are the mean values at $t = 0$ s under 6 and $8 m s^{-1}$ wind speeds. Both β and δ are evaluated based on the slopes for 6 and $8 m s^{-1}$ in Fig. 7. The ambient wind speed is set as $20 m s^{-1}$. The theoretical maximum height of firebrands in self-sustaining burning (Albini 1979) is:

$$H_{max} = 0.39 \times 10^5 D \quad (29)$$

Fig. 13 illustrates the calculated results of the transport model. The burning rate, projected area, relative velocity between firebrands and the surrounding fluid, and firebrand surface temperature are presented in Fig. 13a. The calculated firebrand flight trajectory is indicated in Fig. 13b. The wind speed and transport distance correspond with those in wildfires (Storey et al. 2020a, 2020b). As shown, firebrands with diameters of 15 and 20 mm burned out before landing, whereas the firebrand with a diameter of 25 mm remained burning on landing. The calculated descent trajectory is similar to that in previous work (Lee and Hellman 1970). The maximum flight height is ~ 1 km for diameters of 20 and 25 mm, consistent with Tarifa et al. (1965). The maximum horizontal transport distance is ~ 1600 m, comparable with

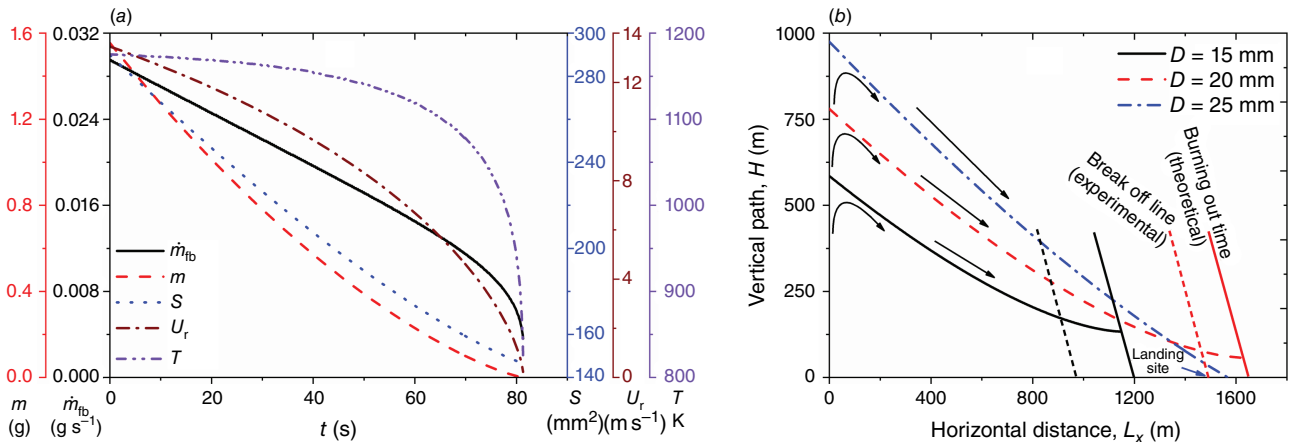


Fig. 13. Transport of firebrands: (a) variations of parameters ($D = 20$ mm); (b) transport trajectory ($U_h = 20 m s^{-1}$).

previous works (Tarifa et al. 1965; Lee and Hellman 1970). It should be noted that the residual mass is zero for calculations, whereas it is non-zero for experiments owing to firebrand breakage. Firebrands in self-sustaining burning may land with flames (Fig. 2) when the relative velocity is less than 6 m s^{-1} , which poses a significant fire hazard in igniting WUI combustibles (Caton et al. 2017; Santoso et al. 2019; Xiong et al. 2020; Wadhvani et al. 2022). The burning and transport of firebrands depend on the relative velocity and direction of the firebrands and the surrounding air flow. Combined with meteorological conditions, the developed models have promising potential for engineering applications.

Conclusions

In this work, wooden firebrand burning was conducted under forced convection. The density, mass, projected area and surface temperature of the firebrands were investigated. A firebrand burning mechanism, including wood pyrolysis and char oxidation, is proposed based on the firebrand density and wind speed. The mass loss due to wood pyrolysis is much greater than that due to char oxidation in self-sustaining burning. Firebrand burning rate is correlated with firebrand diameter, wind speed, pyrolysis rate and flaming or smouldering. The burning rate is proportional to $U^{1/2}$. The reduction rate of the firebrand projected area is correlated with char density, firebrand diameter, wind speed, and flaming or smouldering of firebrands. The projected area for flaming firebrands decreases more rapidly than that for smouldering ones. The surface temperature model is established with firebrand burning rate and wind speed in terms of energy conservation. The firebrand surface temperature is mainly determined by radiation. A simplified firebrand transport model is established to predict the transport trajectory and essential parameters affecting the burning of firebrands.

Nomenclature

B	mass transfer number (–)
c_p	specific heat capacity at constant pressure ($\text{J kg}^{-1} \text{K}^{-1}$)
C_D	drag coefficient (–)
D	firebrand diameter (mm)
D_m	gas diffusivity ($\text{m}^2 \text{s}^{-1}$)
fla	flaming
fb	correction factor (–)
F	force (N)
F_w	drag force of the wind (N)
$F_{y,G}$	force exerted by gravity on the firebrand (N)
$\bar{F}_{y,res}$	air resistance (N)
Δh_{char}	heat of char oxidation (MJ kg^{-1})
h_{conv}	convective heat transfer coefficient ($\text{W m}^{-2} \text{K}^{-1}$)

H	height of the firebrand (m)
K_{film}	thermal conductivity of air ($\text{W m}^{-1} \text{K}^{-1}$)
K_{sol}	thermal conductivity of solid phase ($\text{W m}^{-1} \text{K}^{-1}$)
K	function coefficient (–)
K_1	Stokes' shape factor (–)
K_2	Newton's shape factor (–)
Le	Lewis number (–)
L_x	horizontal transport distance (m)
m_{fb}	firebrand mass (g)
m'_{char}	char oxidation rate (g s^{-1})
Nu	Nusselt number (–)
Pr	Prandtl number (–)
r	firebrand radius (mm)
Re	Reynolds number (–)
smo	smouldering
S	projected area (mm^2)
t	burning time (s)
T_{film}	temperature of gas phase film (K)
T_s	firebrand surface temperature (K)
U	wind speed (m s^{-1})
U_h	horizontal wind speed (m s^{-1})
V_{fb}	firebrand velocity (m s^{-1})
$U_{r,i}$	relative velocity (m s^{-1})
V_x	horizontal speed of firebrand (m s^{-1})
V_y	vertical speed of firebrand (m s^{-1})
Y	mass fraction (–)

Greek symbols

α	thermal diffusion ($\text{m}^2 \text{s}^{-1}$)
α_{fb}^{char}	mass fraction of char in firebrand (–)
β	parameter (–)
δ	parameter (–)
ε_s	emissivity (–)
φ_{pyr}	ratio of wood pyrolysis rate to char oxidation rate (–)
$\bar{\varphi}_{pyr}$	mean ratio of wood pyrolysis rate to char oxidation rate (–)
η	CO-to-CO ₂ ratio (–)
μ	dynamic viscosity (N s m^{-2})
ρ	firebrand density (kg m^{-3})
ρ_g	air density (kg m^{-3})
σ	Stefan–Boltzmann constant ($\text{W m}^{-2} \text{K}^{-4}$)
ζ	stoichiometric coefficient (–)
Ω	firebrand volume (m^3)

Subscripts

bre	firebrand breakage
fe	flame extinction
fla	flaming
smo	smouldering
i	iteration
nc	natural convection
oxi	char oxidation
pyr	wood pyrolysis
s	surface
0	initial value
∞	ambient or infinity

References

- Albini FA (1979) Spot fire distance from burning trees – a predictive model. General Technical Report INT-GTR-56. (USDA Forest Service, Intermountain Forest and Range Experiment Station, Ogden, USA)
- Albini FA (1983) Transport of firebrands by line thermals. *Combustion Science and Technology* 32, 277–288. doi:10.1080/00102208308923662
- Almeida M, Viegas DX, Miranda AI, Reva V (2011) Effect of particle orientation and of flow velocity on the combustibility of *Pinus pinaster* and *Eucalyptus globulus* firebrand material. *International Journal of Wildland Fire* 20, 946–962. doi:10.1071/WF09080
- Anthenien RA, Tse SD, Fernandez-Pello AC (2006) On the trajectories of embers initially elevated or lofted by small scale ground fire plumes in high winds. *Fire Safety Journal* 41, 349–363. doi:10.1016/j.firesaf.2006.01.005
- Caram HS, Amundson NR (1977) Diffusion and reaction in a stagnant boundary layer about a carbon particle. *Industrial & Engineering Chemistry Research* 16, 171–181. doi:10.1021/i160062A001
- Caton SE, Hakes RSP, Gorham DJ, Zhou A, Gollner MJ (2017) Review of pathways for building fire spread in the wildland–urban interface Part I: Exposure conditions. *Fire Technology* 53, 429–473. doi:10.1007/s10694-016-0589-z
- Dal-Ri dos Santos I, Yaghoobian N (2023) Effects of urban boundary layer turbulence on firebrand transport. *Fire Safety Journal* 135, 103726. doi:10.1016/j.firesaf.2022.103726
- Ellis PFM (2013) Firebrand characteristics of the stringy bark of messmate (*Eucalyptus obliqua*) investigated using non-tethered samples. *International Journal of Wildland Fire* 22, 642–651. doi:10.1071/WF12141
- Faeth GM (1977) Current status of droplet and liquid combustion. *Progress in Energy and Combustion Science* 3, 191–224. doi:10.1016/0360-1285(77)90012-0
- Fang W, Peng Z, Chen H (2021) Ignition of pine needle fuel bed by the coupled effects of a hot metal particle and thermal radiation. *Proceedings of the Combustion Institute* 38, 5101–5108. doi:10.1016/j.proci.2020.05.032
- Fernandez-Pello AC (2017) Wildland fire spot ignition by sparks and firebrands. *Fire Safety Journal* 91, 2–10. doi:10.1016/j.firesaf.2017.04.040
- Ganser GH (1993) A rational approach to drag prediction of spherical and nonspherical particles. *Powder Technology* 77, 143–152. doi:10.1016/0032-5910(93)80051-B
- Hall J, Ellis PF, Cary GJ, Bishop G, Sullivan AL (2015) Long-distance spotting potential of bark strips of a ribbon gum (*Eucalyptus viminalis*). *International Journal of Wildland Fire* 24, 1109–1117. doi:10.1071/WF15031
- Himoto K, Tanaka T (2005) Transport of disk-shaped firebrands in a turbulent boundary layer. *Fire Safety Science* 8, 433–444. doi:10.3801/IAFSS.FSS.8-433
- Incropera FP, DeWitt DP, Bergman TL, Lavine AS (2006) *Fundamentals of heat and mass transfer*. 6th edn. (Wiley: New York, NY, USA)
- Knight IK (2001) The design and construction of a vertical wind tunnel for the study of untethered firebrands in flight. *Fire Technology* 37, 87–100. doi:10.1023/A:1011605719943
- Kuo JT, Hwang LH (2003) Mass and thermal analysis of burning wood spheres. *Combustion Science and Technology* 175, 665–693. doi:10.1080/00102200302395
- Lattimer BY, Bearinger E, Wong S, Hodges JL (2022) Evaluation of models and important parameters for firebrand burning. *Combustion and Flame* 235, 111619. doi:10.1016/j.combustflame.2021.111619
- Lee SL, Hellman JM (1969) Study of firebrand trajectories in a turbulent swirling natural convection plume. *Combustion and Flame* 13, 645–655. doi:10.1016/0010-2180(69)90072-8
- Lee SL, Hellman JM (1970) Firebrand trajectory study using an empirical velocity-dependent burning law. *Combustion and Flame* 15, 265–274. doi:10.1016/0010-2180(70)90006-4
- Manzello SL (2020) Introduction to the special section on global overview of large outdoor fire standards. *Fire Technology* 56, 1827–1829. doi:10.1007/s10694-020-00962-6
- Manzello SL, Suzuki S, Gollner MJ, Fernandez-Pello AC (2020) Role of firebrand combustion in large outdoor fire spread. *Progress in Energy and Combustion Science* 76, 100801. doi:10.1016/j.pecc.2019.100801
- Mell WE, Manzello SL, Maranghides A, Butry D, Rehm RG (2010) The wildland–urban interface fire problem – current approaches and research needs. *International Journal of Wildland Fire* 19, 238–251. doi:10.1071/WF07131
- Mukunda HS, Paul PJ, Srinivasa U, Rajan NKS (1985) Combustion of wooden spheres – experiments and model analysis. *Symposium (International) on Combustion* 20, 1619–1628. doi:10.1016/S0082-0784(85)80657-3
- Oliveira LA, Lopes AG, Baliga BR, Almeida M, Viegas DX (2014) Numerical prediction of size, mass, temperature and trajectory of cylindrical wind-driven firebrands. *International Journal of Wildland Fire* 23, 698–708. doi:10.1071/WF13080
- Sardoy N, Consalvi JL, Porterie B, Kaiss A (2006) Transport and combustion of ponderosa pine firebrands from isolated burning trees. In ‘First International Symposium on Environment Identities and Mediterranean Area’, 2006. ISEIMA ‘06’, 9–12 July 2006, Corte-Ajaccio, France. pp. 6–11. (Institute of Electrical and Electronics Engineers: New York, USA) doi:10.1109/ISEIMA.2006.345036
- Pagni PJ (1981) Diffusion flame analyses. *Fire Safety Journal* 3, 273–285. doi:10.1016/0379-7112(81)90049-7
- Porteiro J, Granada E, Collazo J, Patiño D, Morán JC (2007) A model for the combustion of large particles of densified wood. *Energy & Fuels* 21, 3151–3159. doi:10.1021/ef0701891
- Santoso MA, Christensen EG, Yang J, Rein G (2019) Review of the transition from smouldering to flaming combustion in wildfires. *Frontiers in Mechanical Engineering* 5, 49. doi:10.3389/fmech.2019.00049
- Sardoy N, Consalvi JL, Porterie B, Fernandez-Pello AC (2007) Modeling transport and combustion of firebrands from burning trees. *Combustion and Flame* 150, 151–169. doi:10.1016/j.combustflame.2007.04.008
- Song J, Huang X, Liu N, Li H, Zhang L (2017) The wind effect on the transport and burning of firebrands. *Fire Technology* 53, 1555–1568. doi:10.1007/s10694-017-0647-1
- Spalding DB (1953) The combustion of liquid fuels. *Symposium (International) on Combustion* 4, 847–864. doi:10.1016/S0082-0784(53)80110-4
- Storey MA, Price OF, Bradstock RA, Sharples JJ (2020a) Analysis of variation in distance, number, and distribution of spotting in south-east Australian wildfires. *Fire* 3, 10. doi:10.3390/fire3020010
- Storey MA, Price OF, Sharples JJ, Bradstock RA (2020b) Drivers of long-distance spotting during wildfires in south-eastern Australia. *International Journal of Wildland Fire* 29, 459–472. doi:10.1071/WF19124
- Suzuki S, Manzello SL, Kagiya K, Suzuki J, Hayashi Y (2015) Ignition of mulch beds exposed to continuous wind-driven firebrand showers. *Fire Technology* 51, 905–922. doi:10.1007/s10694-014-0425-2
- Tarifa CS, Notario PP, Moreno FG (1965) On the flight paths and lifetimes of burning particles of wood. *Symposium (International) on Combustion* 10, 1021–1037. doi:10.1016/s0082-0784(65)80244-2
- Thunman H, Leckner B, Niklasson F, Johnsson F (2002) Combustion of wood particles – a particle model for Eulerian calculations. *Combustion and Flame* 129, 30–46. doi:10.1016/S0010-2180(01)00371-6
- Tse SD, Fernandez-Pello AC (1998) On the flight paths of metal particles and embers generated by power lines in high winds – a potential source of wildland fires. *Fire Safety Journal* 30, 333–356. doi:10.1016/S0379-7112(97)00050-7
- Turns S (2000) *An introduction to combustion concepts and applications*. (McGraw Hill: Boston, MA, USA)
- Urban JL, Fernandez-Pello AC, Vicariotto M, Dunn-Rankin D (2019a) Temperature measurement of glowing embers with color pyrometry. *Fire Technology* 55, 1013–1026. doi:10.1007/s10694-018-0810-3
- Urban JL, Song J, Santamaria S, Fernandez-Pello AC (2019b) Ignition of a spot smolder in a moist fuel bed by a firebrand. *Fire Safety Journal* 108, 102833. doi:10.1016/j.firesaf.2019.102833
- Wadhvani R, Sullivan C, Wickramasinghe A, Kyng M, Khan N, Moinuddin K (2022) A review of firebrand studies on generation and transport. *Fire Safety Journal* 134, 103674. doi:10.1016/j.firesaf.2022.103674
- Wong S, Hodges JL, Lattimer BY (2022) Impact of ash layer retention on heat transfer in piles of vegetation and structure firebrands. *Fire Safety Journal* 134, 103694. doi:10.1016/j.firesaf.2022.103694

- Woycheese JP, Pagni PJ (1999) Combustion models for wooden brands. In 'Proceedings of 3rd International Conference on Fire Research and Engineering (ICFRE3)', 4–8 October 1999, Chicago, IL. pp. 53–71. (Boston, MA, USA)
- Woycheese JP, Pagni PJ, Liepmann D (1999) Brand propagation from large-scale fires. *Journal of Fire Protection Engineering* 10, 32–44. doi:10.1177/104239159901000203
- Xiong C, Liu Y, Xu C, Huang X (2020) Acoustical extinction of flame on moving firebrand for the fire protection in wildland-urban interface. *Fire Technology* 57, 1365–1380. doi:10.1007/s10694-020-01059-w
- Zhu H, Liu N (2020) Thermal decomposition of biomass and shallow soil mixtures. *Fire Safety Journal* 113, 102990. doi:10.1016/j.firesaf.2020.102990

Data availability. Data that support this study will be shared upon reasonable request to the corresponding author.

Conflicts of interest. Dr Naian Liu is an Associate Editor of the International Journal of Wildland Fire. All authors hereby declare that they do not have any conflict of interest, and have participated in (a) experimental design, and analysis of the data; (b) drafting the article or revising it critically for important intellectual content; and (c) approval of the final version. This manuscript has not been submitted to, nor is under review at another journal or other publishing venue. The authors have no affiliation with any organisation with a direct or indirect financial interest in the subject matter discussed in the manuscript.

Declaration of funding. This research is sponsored by the National Key Research and Development Plan (No. 2022YFC3003000), the National Natural Science Foundation of China (Nos. 52321003 and 51936011), the China Postdoctoral Science Foundation (2021M703083) and the Foundation of State Key Laboratory of Laser Interaction with Matter (SKLLIM2001).

Acknowledgements. We thank the following people for help in the laboratory: Fengkai Liu and Hongming Zhang for general advice and help.

Author affiliations

^AState Key Laboratory of Fire Science, University of Science and Technology of China, Hefei, Anhui 230026, China.

^BMinistry of Emergency Management Key Laboratory of Forest Fire Monitoring and Warning, University of Science and Technology of China, Hefei 230026, China.